Electronic Supplementary Material (ESI) for Journal of Materials Chemistry A.

Supporting Information

Hierarchical Co/MoNi Heterostructure Grown on Monocrystalline $CoNiMoO_x$ Nanorods with Robust Bifunctionality for Hydrazine-oxidation-assisted Energy-saving Hydrogen Evolution

Zehao Xiao,[a] Jie Wang,[c] Hongxiu Lu,[a] Yinyin Qian,[b] Qiang Zhang,[c] Aidong Tang,*[a, b] Huaming Yang*[b, c]

[a] College of Chemistry and Chemical Engineering, Central South University, Changsha, 410083, China

[b] Engineering Research Centre of Nano-geomaterials of Ministry of Education, China University of Geoscience, Wuhan, 430074, China

[c] Hunan Key Lab of Mineral Materials and Application, School of Minerals Processing and Bioengineering, Central South University, Changsha, 410083, China

*Corresponding E-mail: adtang@csu.edu.cn (A. Tang) and hmyang@csu.edu.cn (H. Yang)

Materials

$Co(NO_3)_2 \cdot 6H_2O$, $(NH_4)_6Mo_7O_{24} \cdot 2H_2O$, NaOH, hydrazine hydrate ($N_2H_4 \cdot H_2O$), sodium chloride (NaCl), ethanol and hydrochloric acid were purchased from Sinopharm China and used without further purification. Nickel foams (NF, 1.5 mm thickness, 350 $g \cdot cm^{-2}$ areal density) were purchased from Kunshan Lvchuang Technology Co. Ltd in China. De-ionized (DI, 18.2 $\Omega \cdot cm^{-1}$) water used in all experiments was standard solutions.

Synthesis of 20 wt% Pt/C/NF

The mixture of 10 mg commercial 20 wt% Pt/C powders, 500 μL ethanol, 460 μL water and 40 μL Nafion were uniformly dispersed under ultra-sonication for 1 h. Then, above homogeneous solution was slowly dropped into the cleaning NF and dried in air to synthesis the 20 wt% Pt/C/NF catalyst.

Turnover frequency (TOF) calculation

TOF reflects the reactants at per active site per time.We assume that all active sites are fully exposed to the electrolyte. The number of active sites for as-prepared samples are calculated using the following equation:

$$n = Q / (2 \times F)$$

Where F is the Faraday constant (96485 $C \cdot mol^{-1}$) and Q is the number of voltammetry charge from the cyclic voltammetry (CV) curves as shown in Figure S22. The per-site TOF can be calculated from the following equation:

$$TOF = I / (2 \times n \times F)$$

Where I is the measured current density which can be obtained from linear sweep voltammetry (LSV) polarization curves, F is the Faraday constant (96485 $C \cdot mol^{-1}$), and n is the amount of the active sites.

Electrochemical active surface area (ECSA) calculation

CV curves are measured under different scan rates in the non-Faradaic region. The electrochemical double layer capacitance (C_{dl}) closely relates to ECSA, which is estimated by plotting the charging current differences $\Delta_j = (j_a - j_c)$ where the slope of the linear fits the twice of C_{dl} under different scan rates. C_{dl} thus could be calculated from the following equation:

$$j = S \times C_{dl} \times v$$

Where j is the half of double layered capacitive current density ($mA \cdot cm^{-2}$), S is the tested area of the electrode (1.0 cm^2), and v is the scan rate ($mV \cdot s^{-1}$).

Computational details

The first-principles were employed to perform all density functional theory (DFT) calculations within the generalized gradient approximation (GGA) through the Perdew-Burke-Ernzerhof (PBE) formulation.[1-3] The projected augmented wave (PAW) potentials were chosen to describe the ionic cores and take valence electrons into account using a plane wave basis set with the cutoff energy of 400 eV.[4, 5] Partial occupancies of the Kohn-Sham orbitals were allowed using the Gaussian smearing method with the width of 0.05 eV. The electronic energy was considered self-consistent when the energy change was smaller than 10^{-6} eV. A geometry optimization was considered convergent when the energy change was smaller than 0.05 eV·Å^{-1}. The vacuum spacing in the direction perpendicular to the plane of the structure was 18 Å for the surface of NiMo (133) and Co (101). The Brillouin zone integration was performed using 2 × 2 × 1 Monkhorst-Pack k-point sampling for each structure. Finally, the adsorption energies (E_{ads}) were calculated from the following equation:

$$E_{ads} = E_{ad/sub} - E_{ad} - E_{sub}$$

Where $E_{ad/sub}$, E_{ad}, and E_{sub} are the total energies of the optimized adsorbate/substrate system, the adsorbate in the structure and the clean substrate, respectively.

The free energy is calculated from the following equation:

$$G = E_{ads} + ZPE - TS$$

Where G, E_{ads}, ZPE and TS are the free energy, total energy from DFT calculations, zero point energy and entropic contributions, respectively.

The transition state of an elementary reaction step was located by the (Nudged Elastic Band, NEB) method for the H_2O decomposition step. In the NEB method, the path between reactant (s) and product (s) was discretized into a series of free structural images. Intermediate images were relaxed until the perpendicular forces were lower than 0.05 eV·Å^{-1}. Finally, reaction energies (G) of different intermediates were calculated from the following equation:

$$G = G_i - G_{reactant}$$

Where G_i is the energy of intermediates and $G_{reactant}$ is the total energy of reactants, respectively.

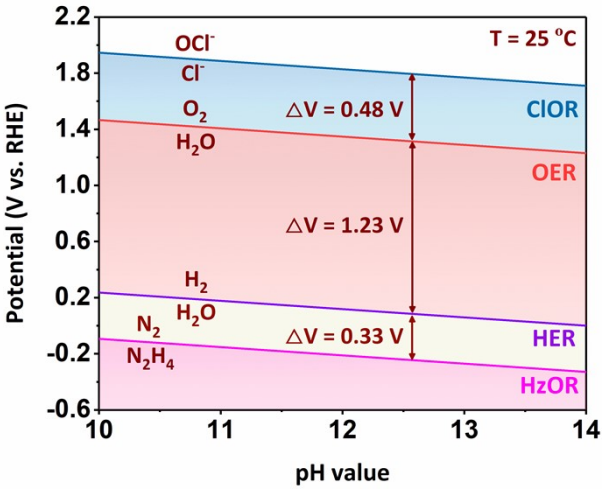

Figure S1. Pourbaix diagram of HzOR, HER, OER, and ClOR under different pH values.

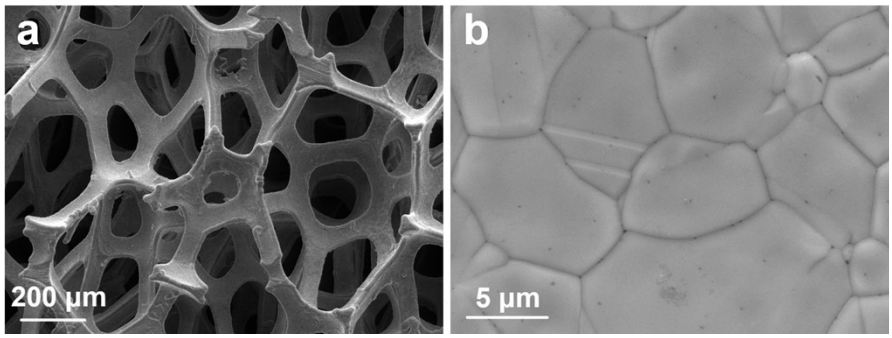

Figure S2. SEM images of the bare NF substrate.

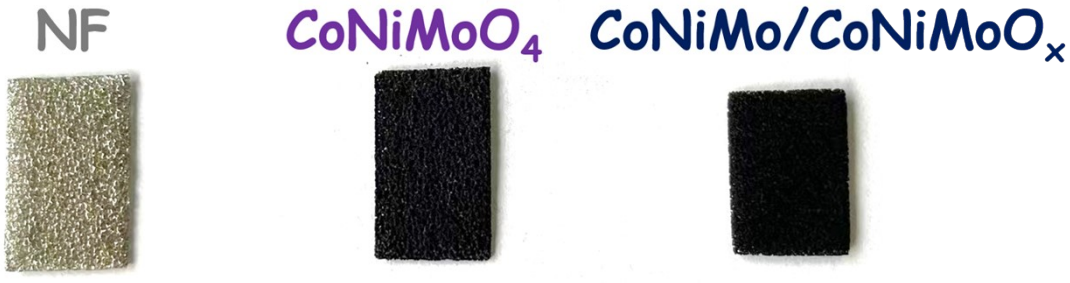

Figure S3. Digital images of the NF, $CoNiMoO_4$ and $CoNiMo/CoNiMoO_x$.

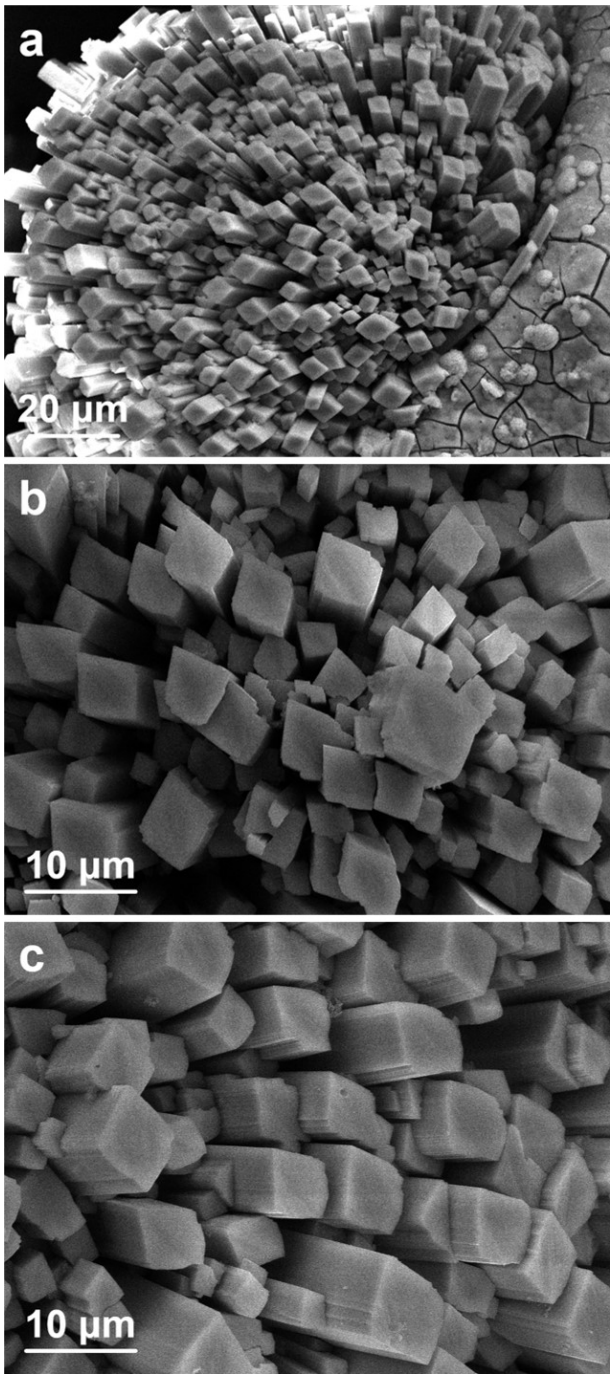

Figure S4. SEM images of the $CoNiMoO_4$ precursor.

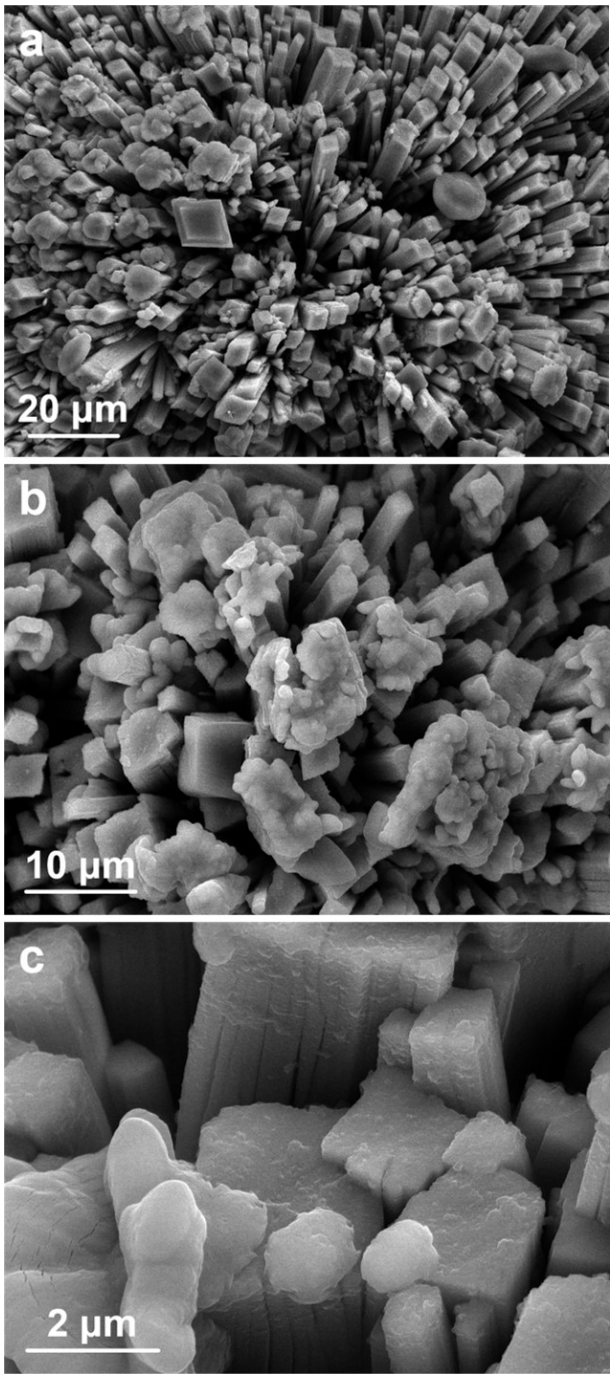

Figure S5. SEM images of the CoNiMo/CoNiMoO_x catalyst.

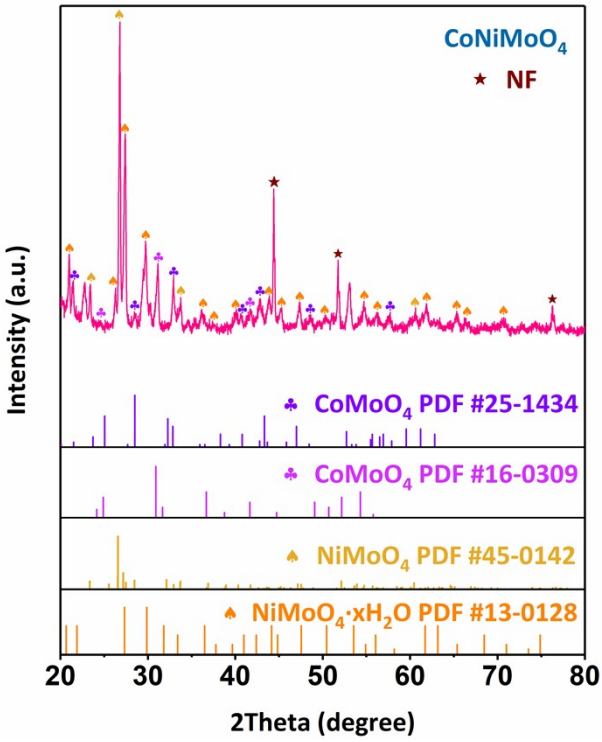

Figure S6. XRD pattern of the $CoNiMoO_4$ precursor.

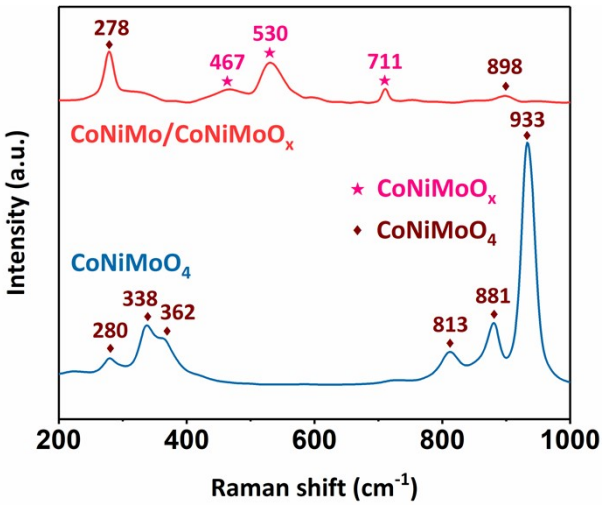

Figure S7. Raman spectra of $CoNiMoO_4$ and $CoNiMo/CoNiMoO_x$.

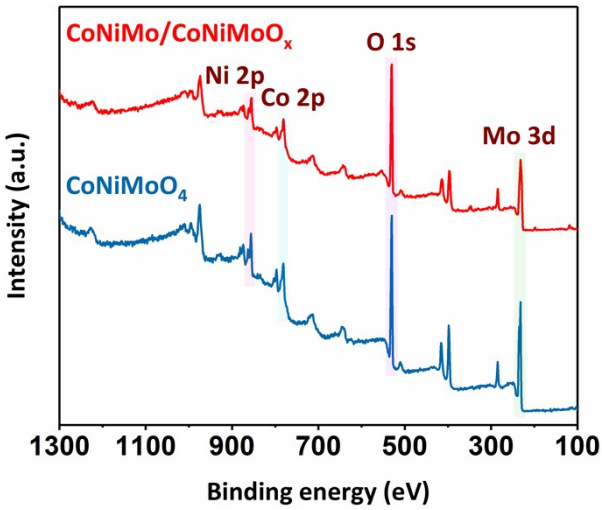

Figure S8. XPS survey spectrum of $CoNiMoO_4$ and $CoNiMo/CoNiMoO_x$.

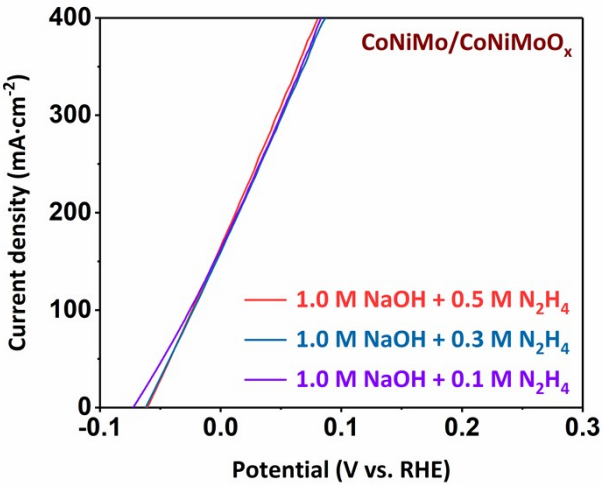

Figure S9. HzOR LSV curves of the $CoNiMo/CoNiMoO_x$ catalyst in 1.0 M NaOH with various hydrazine concentrations.

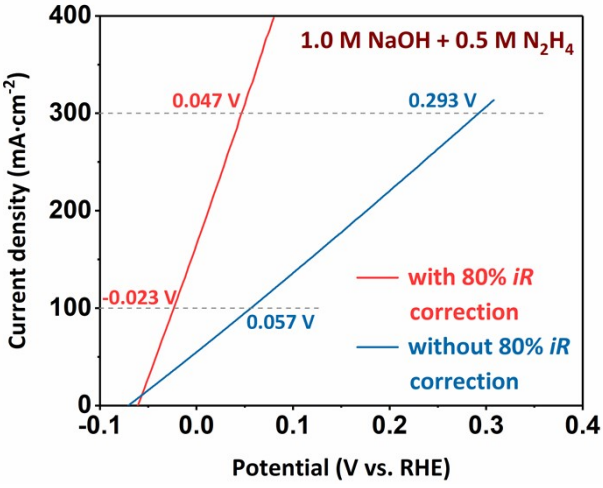

Figure S10. HzOR LSV curves of the $CoNiMo/CoNiMoO_x$ with/without 80% *iR* correction.

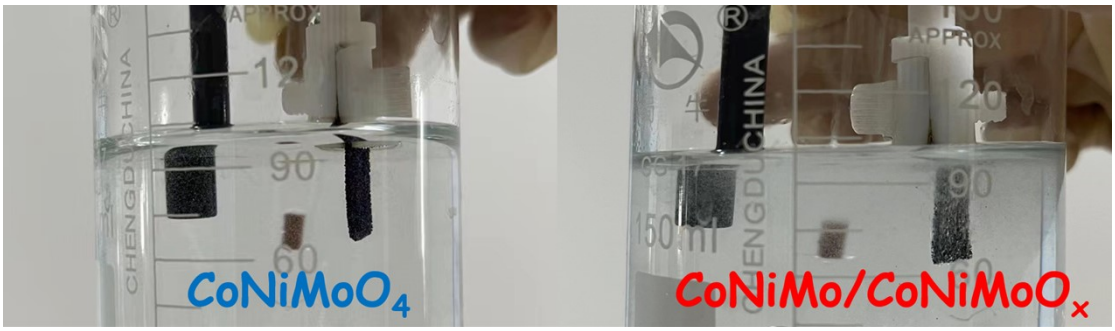

Figure S11. Digital images of $CoNiMoO_4$ and $CoNiMo/CoNiMoO_x$ in the solution of 1.0 M NaOH with 0.5 M N_2H_4 at the open circuit potential.

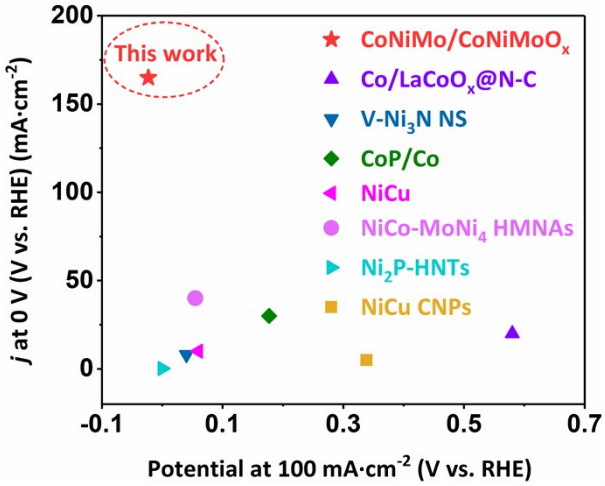

Figure S12. Comparison of catalytic activities with recently reported HzOR catalysts. The details can be found in **Table S1**.

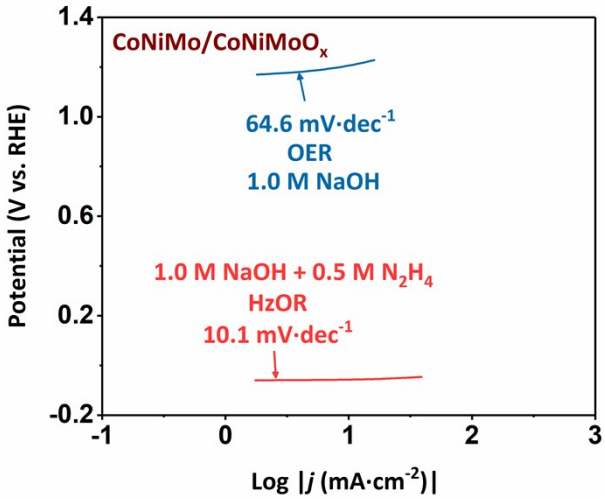

Figure S13. Comparison of Tafel plos between HzOR with OER of the $CoNiMo/CoNiMoO_x$ catalyst in different electrolytes.

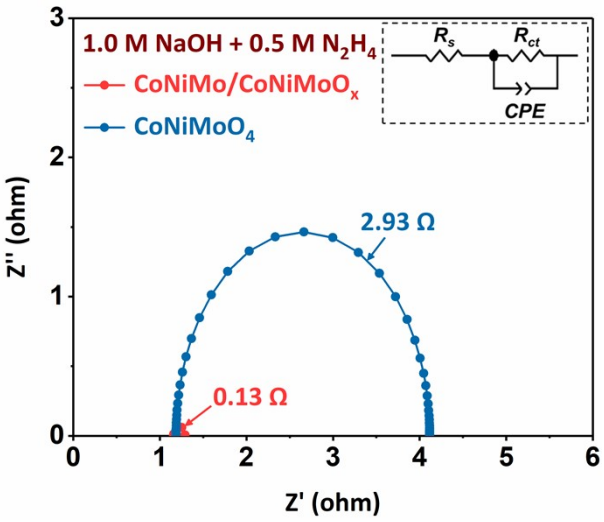

Figure S14. Nyquist plots of $CoNiMoO_4$ and $CoNiMo/CoNiMoO_x$ for HzOR at 10 mV (vs. RHE).

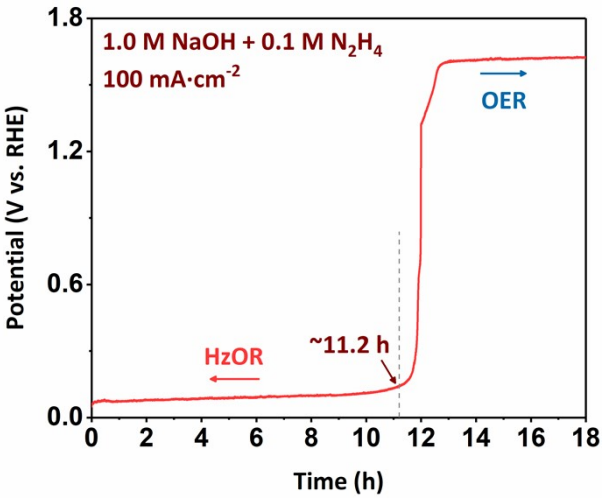

Figure S15. Durability test of the $CoNiMo/CoNiMoO_x$ catalyst at current density of 100 $mA \cdot cm^{-2}$ under 1.0 M NaOH with 0.1 M N_2H_4 to evaluate the removal rate of N_2H_4.

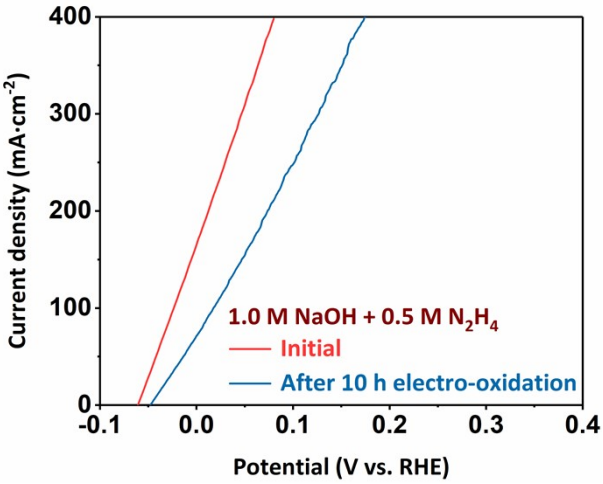

Figure S16. The comparison of HzOR LSV curves for the CoNiMo/CoNiMoO$_x$ catalyst (initial state, red line) and CoNiMo/CoNiMoO$_x$ catalyst (after 10 h electro-oxidation at 100 mA·cm^{-2} under 1.0 M KOH, blue line).

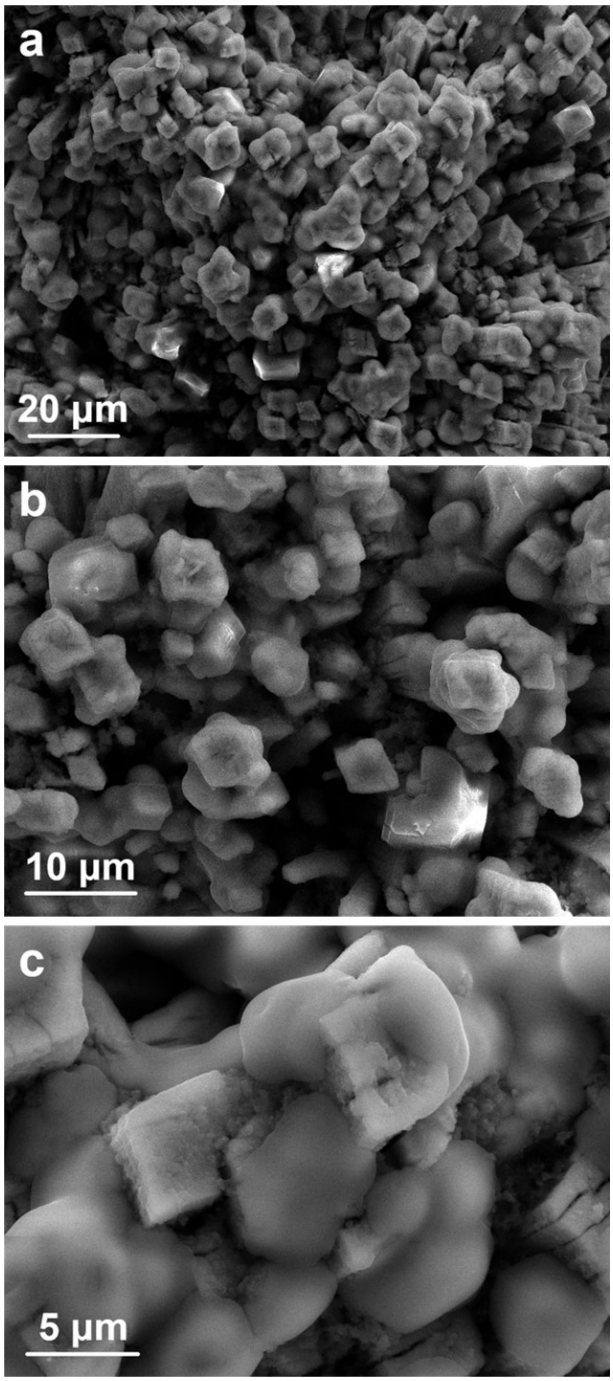

Figure S17. SEM images of the CoNiMo/CoNiMoO_x catalyst after 60 h HzOR stability test.

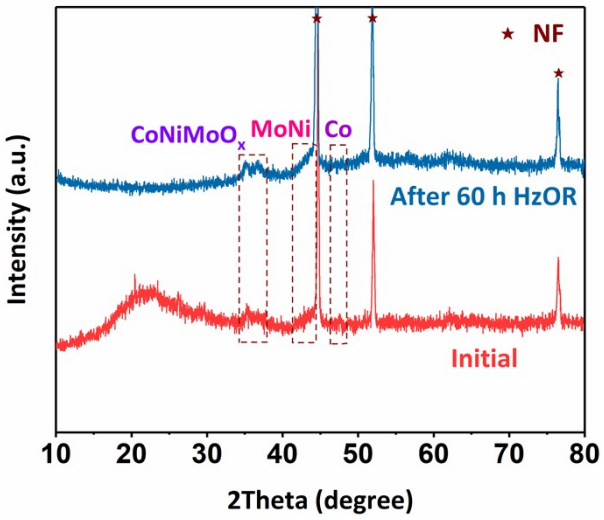

Figure S18. XRD pattern of the CoNiMo/CoNiMoO$_x$ catalyst before and after 60 h HzOR stability test.

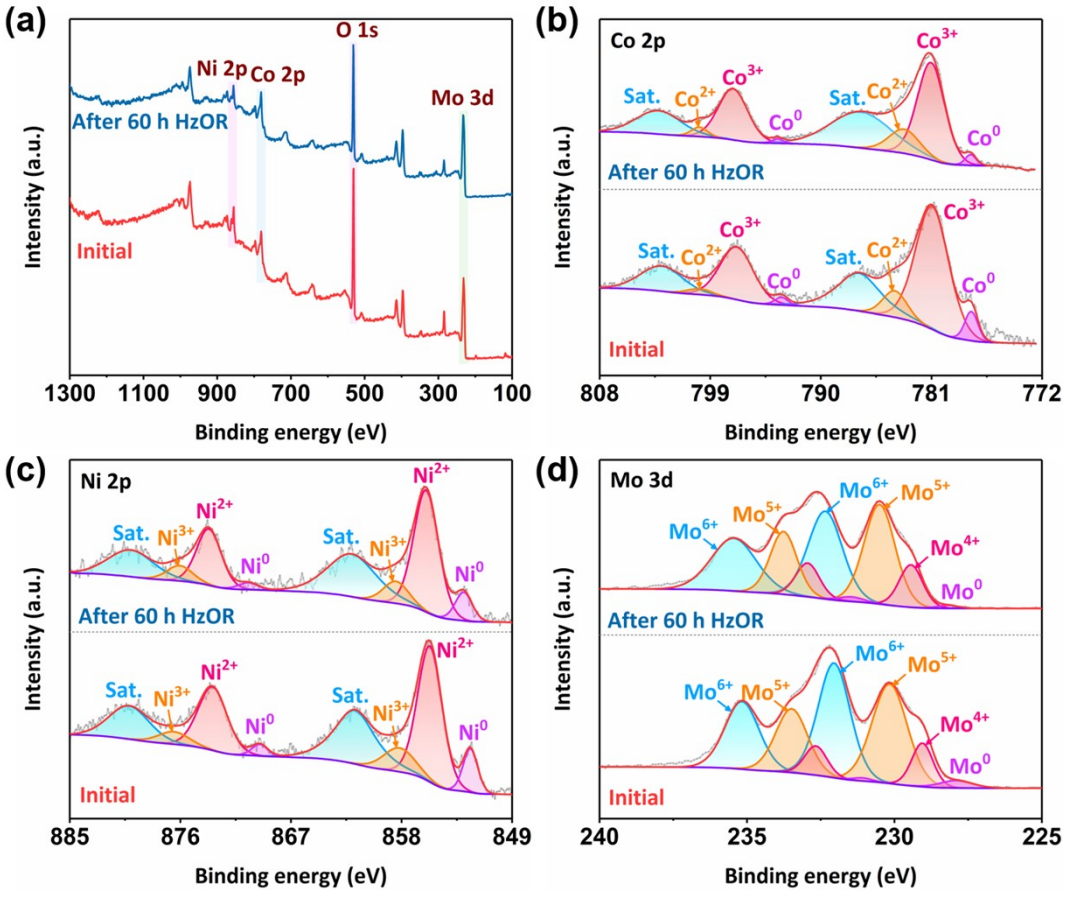

Figure S19. XPS spectrum of the CoNiMo/CoNiMoO$_x$ catalyst before and after 60 h HzOR stability test.

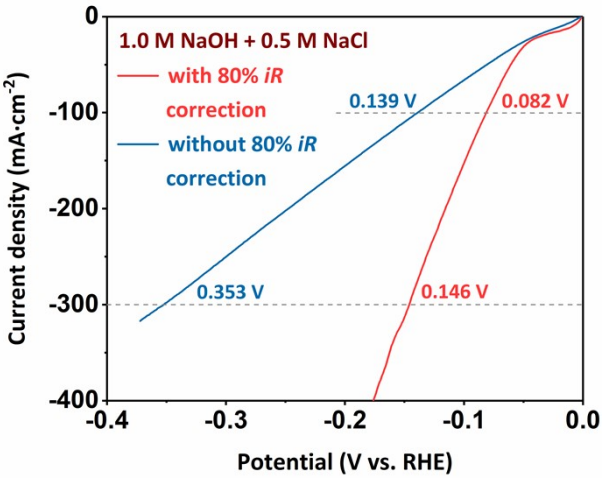

Figure S20. HER LSV curves of the CoNiMo/CoNiMoO$_x$ catalyst with/without 80% *iR* correction.

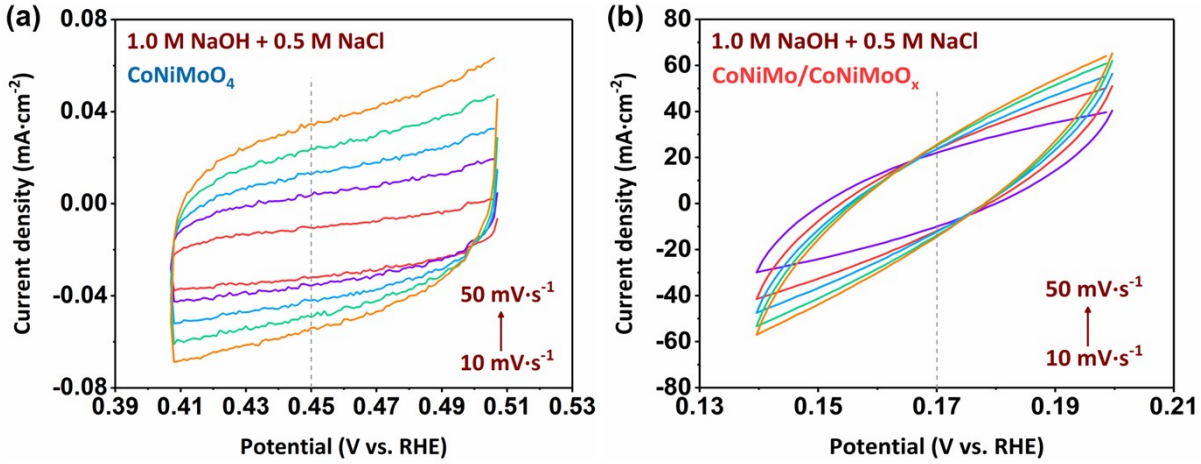

Figure S21. CV curves of CoNiMoO$_4$ and CoNiMo/CoNiMoO$_x$ under different scan rates in the non-Faradic region.

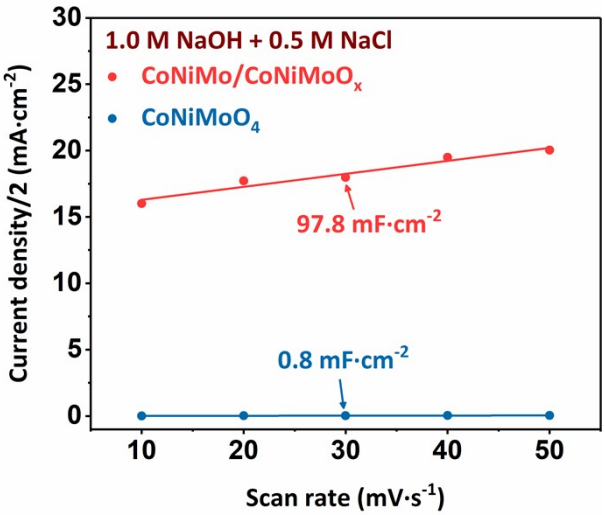

Figure S22. Linear dependence of capacitive current density of $CoNiMoO_4$ and $CoNiMo/CoNiMoO_x$ to calculate C_{dl} value.

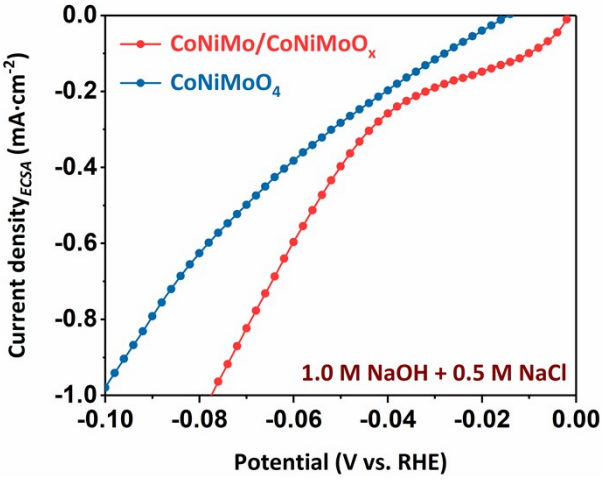

Figure S23. HER LSV curves of $CoNiMoO_4$ and $CoNiMo/CoNiMoO_x$ normalized by the electrochemical active surface area (ECSA).

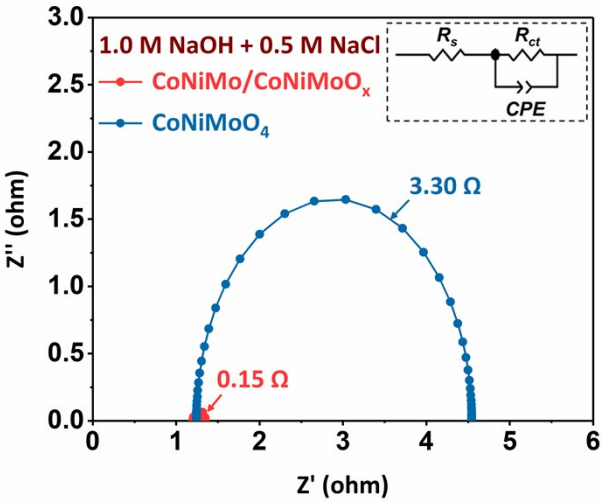

Figure S24. Nyquist plots of $CoNiMoO_4$ and $CoNiMo/CoNiMoO_x$ for HER at the overpotential of 50 mV.

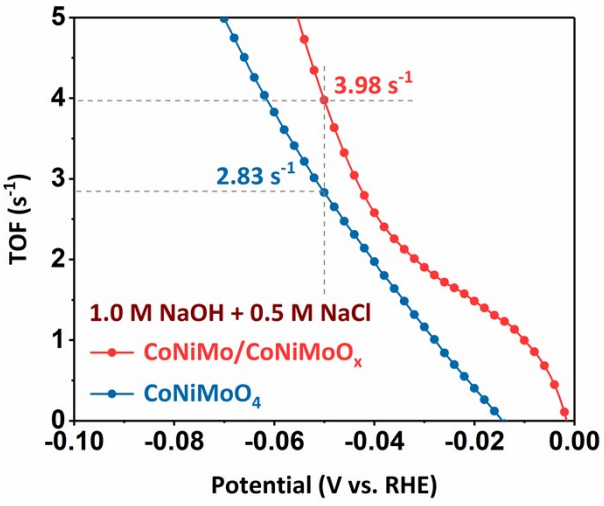

Figure S25. TOF values of $CoNiMoO_4$ and $CoNiMo/CoNiMoO_x$ varying with different overpotentials.

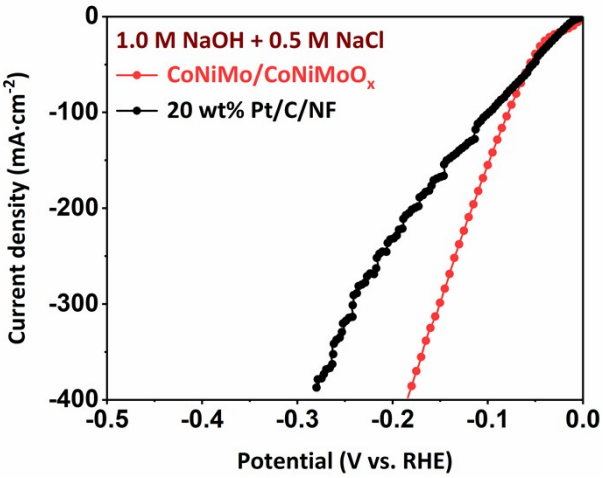

Figure S26. HER LSV curves of 20 wt% Pt/C/NF and CoNiMo/CoNiMoO$_x$ in 1.0 M NaOH with 0.5 M NaCl.

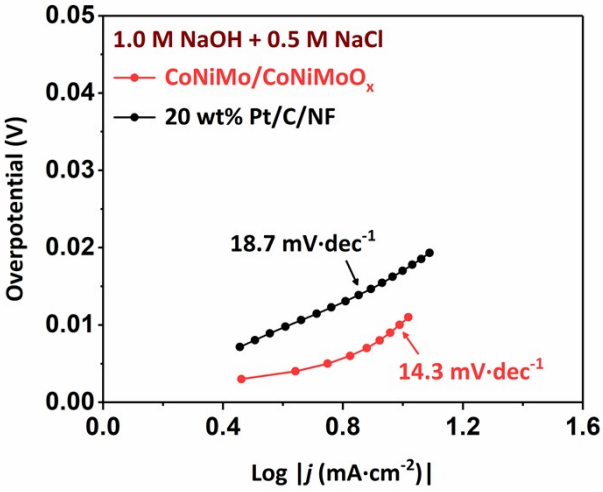

Figure S27. Tafel plots of 20 wt% Pt/C/NF and CoNiMo/CoNiMoO$_x$ in 1.0 M NaOH with 0.5 M NaCl.

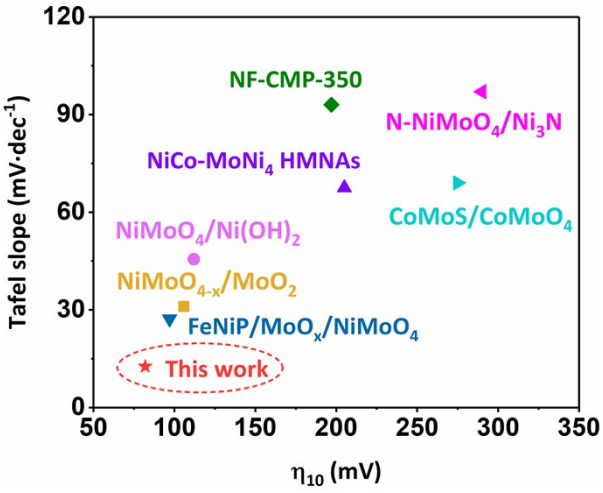

Figure S28. Comparison of catalytic activities with recently reported HER catalysts. The details can be found in **Table S2**.

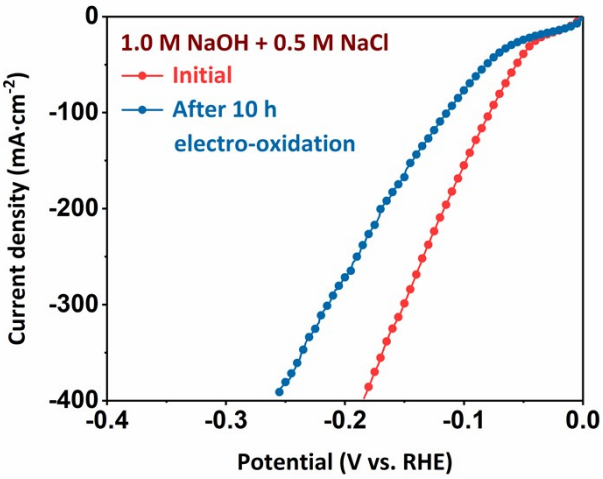

Figure S29. The comparison of HER LSV curves for the CoNiMo/CoNiMoO$_x$ catalyst (initial state, red line) and CoNiMo/CoNiMoO$_x$ catalyst (after 10 h electro-oxidation at 100 mA·cm^{-2} under 1.0 M KOH, blue line).

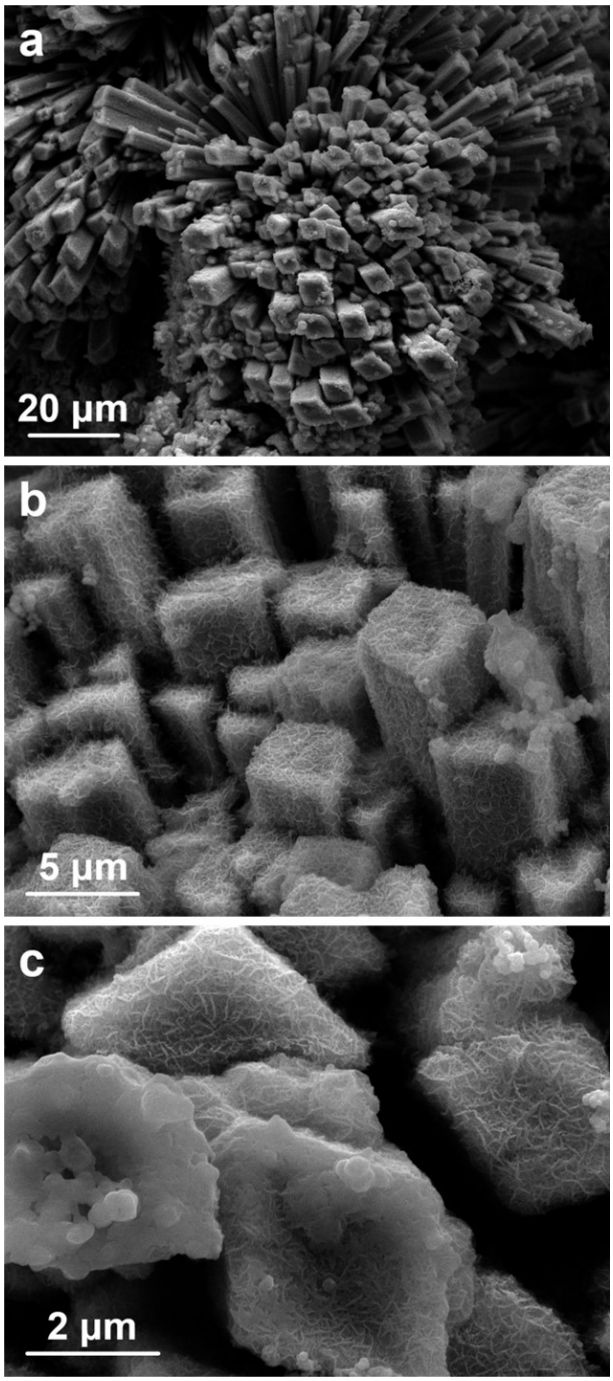

Figure S30. SEM images of the CoNiMo/CoNiMoO_x catalyst after 100 h HER.

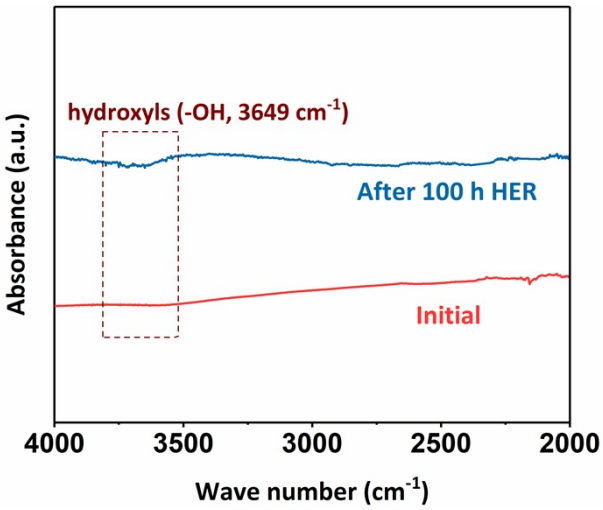

Figure S31. FTIR spectra of the CoNiMo/CoNiMoO$_x$ catalyst before and after 100 h HER.

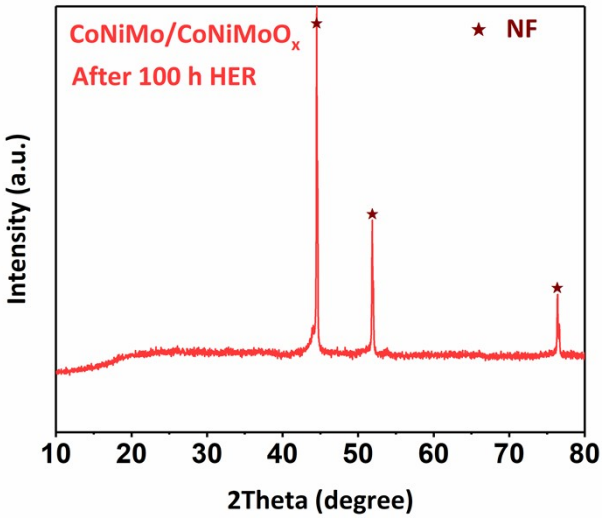

Figure S32. XRD pattern of the CoNiMo/CoNiMoO$_x$ catalyst after 100 h HER.

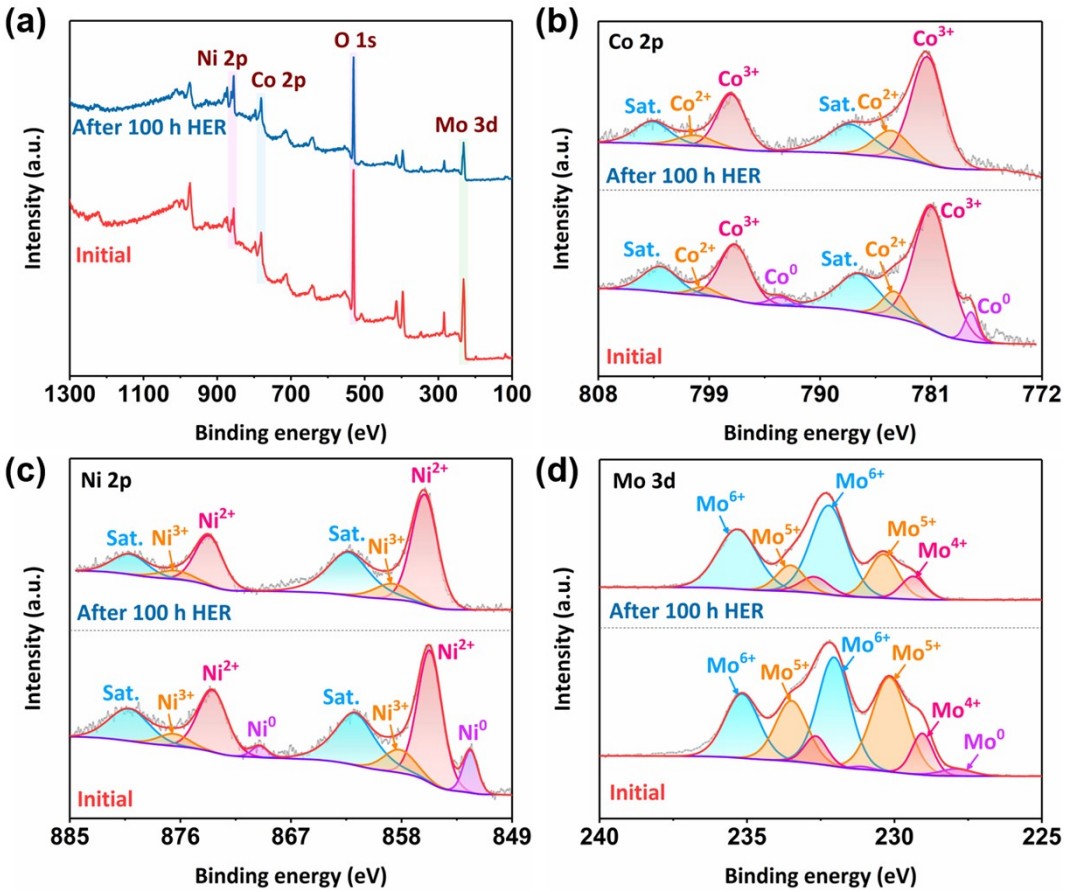

Figure S33. XPS spectrum of the CoNiMo/CoNiMoO$_x$ catalyst before and after 100 h HER.

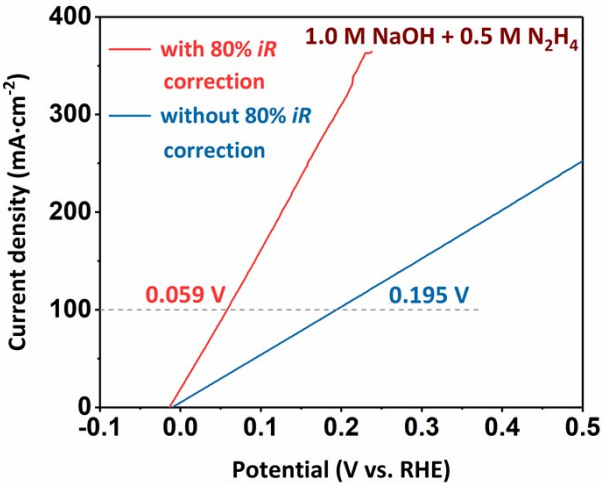

Figure S34. LSV curves of the CoNiMo/CoNiMoO$_x$ electrode assembled hybrid seawater electrolyzer coupling seawater reduction and HzOR with/without 80% *iR* correction.

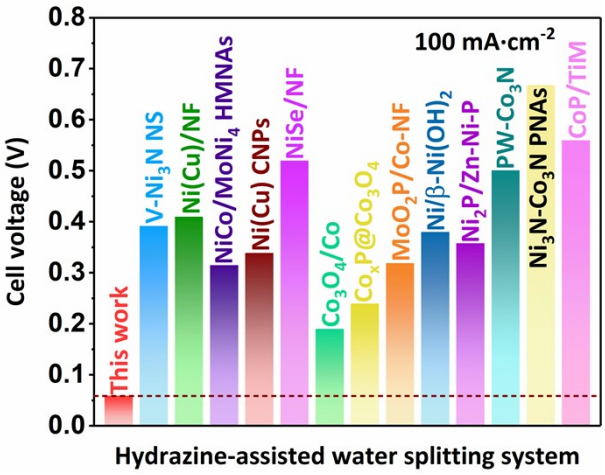

Figure S35. The comparison of the CoNiMo/CoNiMoO$_x$ catalyst assembled hybrid seawater electrolyzer coupling seawater reduction and HzOR with recently reported hydrazine-assisted water splitting systems.

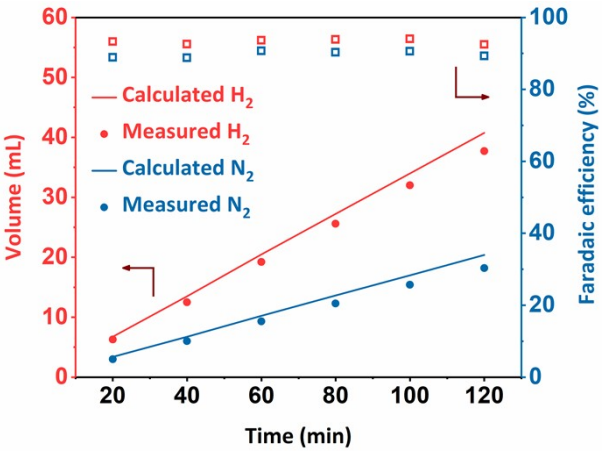

Figure S36. The Faradaic efficiency of the CoNiMo/CoNiMoO$_x$ electrode assembled hybrid seawater electrolyzer coupling seawater reduction and HzOR under current density of 50 mA·cm^{-2}.

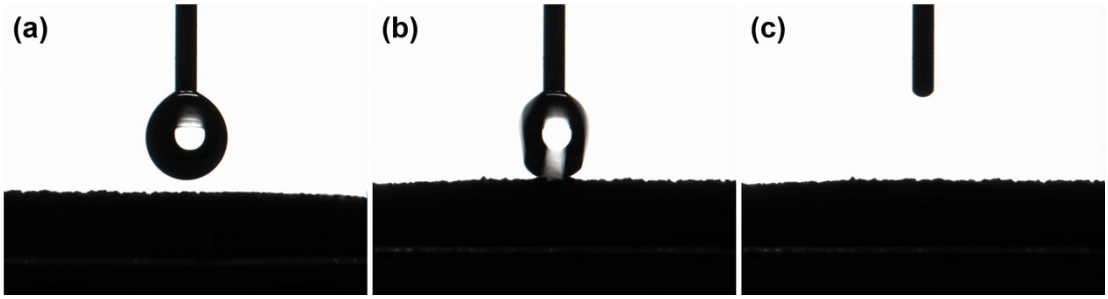

Figure S37. The wetting contact angle measurement with a drop of water on the surface of the CoNiMo/CoNiMoO$_x$ catalyst at (a) 0 s, (b) 0.008 s and (c) 0.012 s.

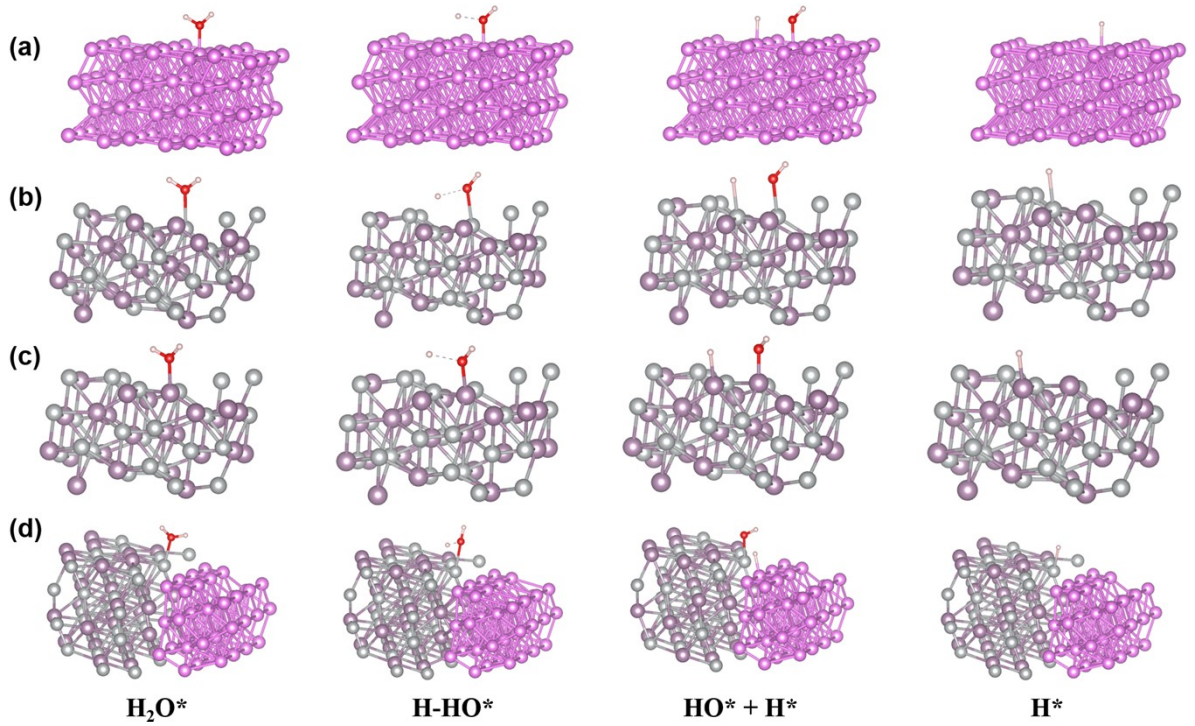

Figure S38. Intermediates during HER for (a) Co (101), (b) MoNi (133, H_2O adsroded on the Mo site), (c) MoNi (133, H_2O adsroded on the Ni site) and (d) the Co/MoNi heterostructure.

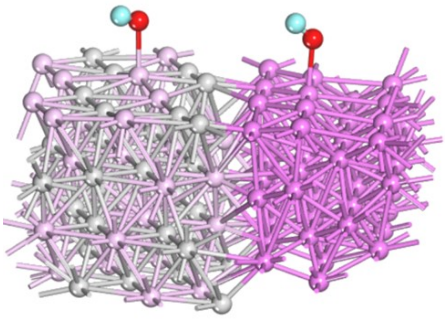

Figure S39. Side-view of structure model for the Co-OH*/MoNi-OH* heterostructure.

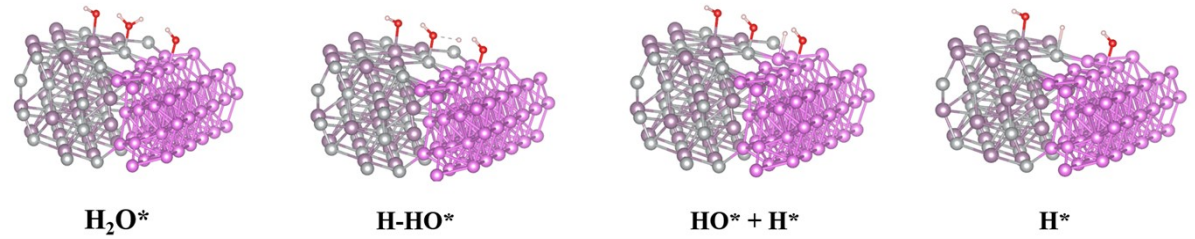

Figure S40. Intermediates during HER for the Co-OH*/MoNi-OH* heterostructure.

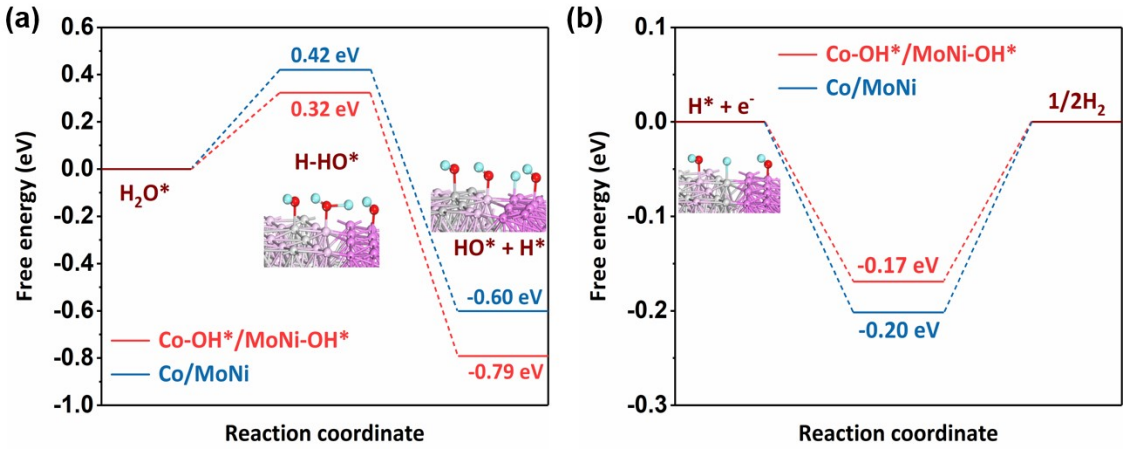

Figure S41. Free-energy barriers of water dissociation and hydrogen adsorption over Co-OH*/MoNi-OH*.

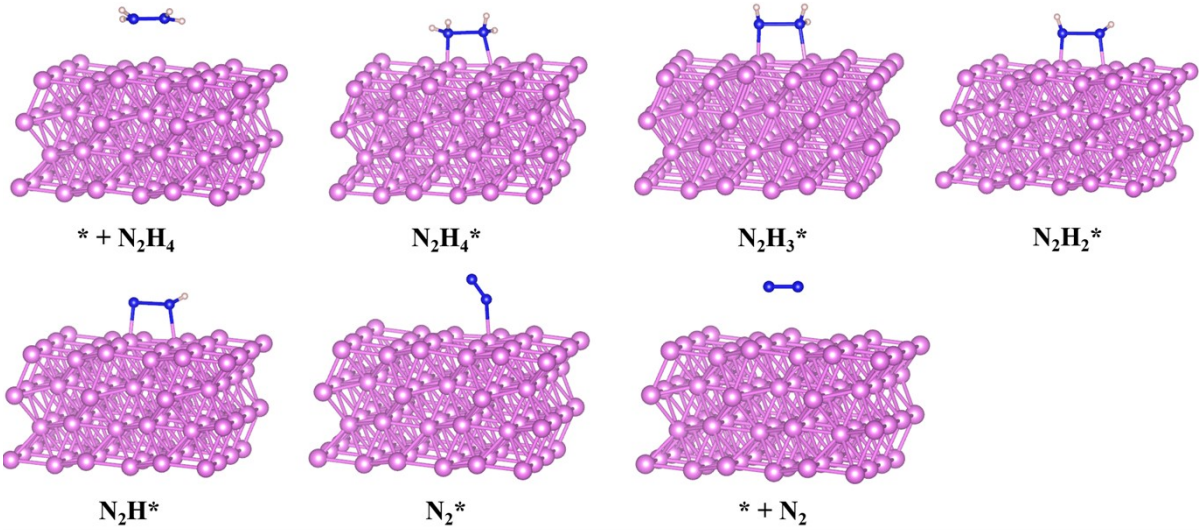

Figure S42. Intermediates during HzOR for Co (101).

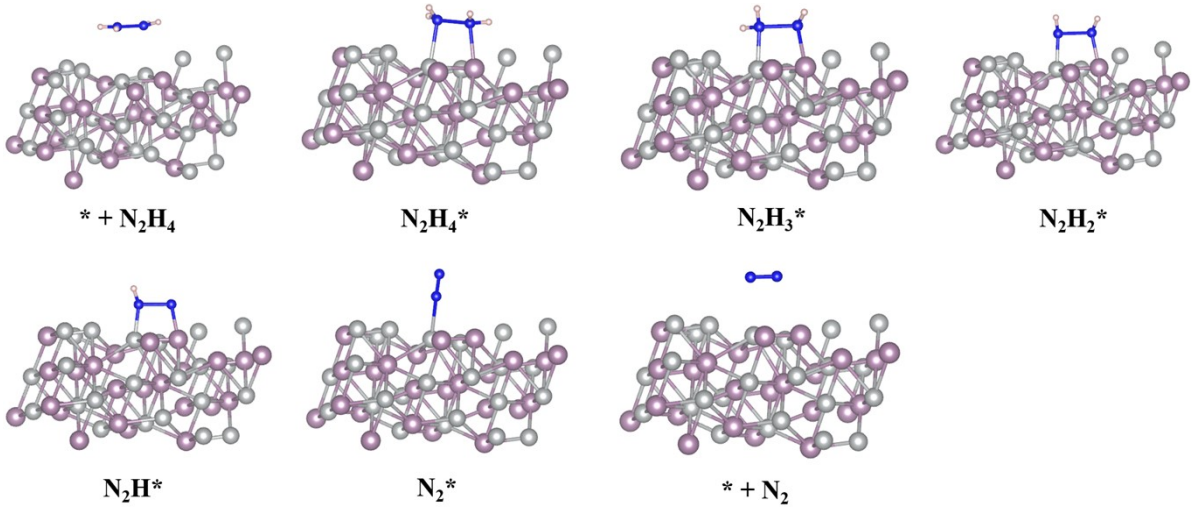

Figure S43. Intermediates during HzOR for MoNi (133).

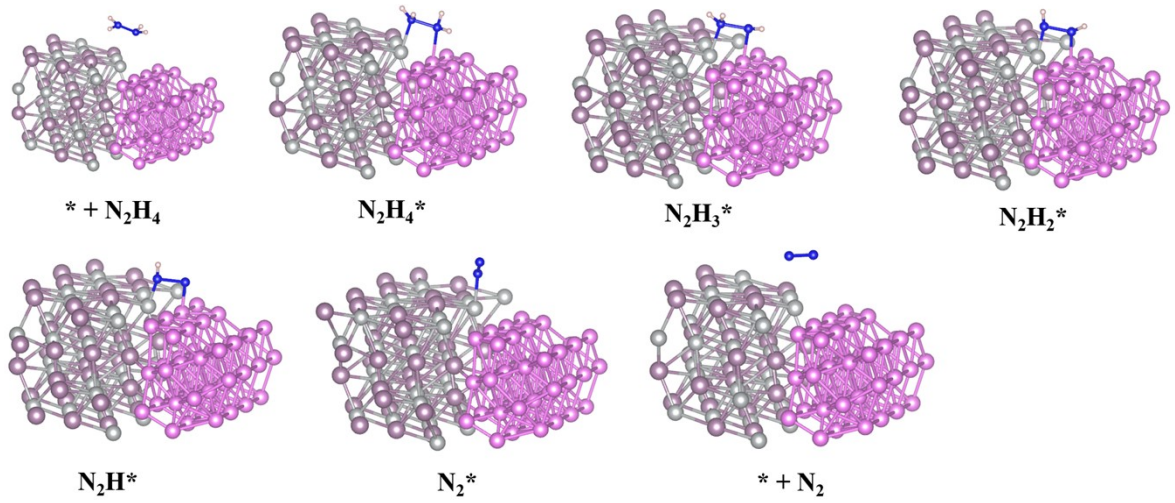

Figure S44. Intermediates during HzOR for the Co/MoNi heterostructure.

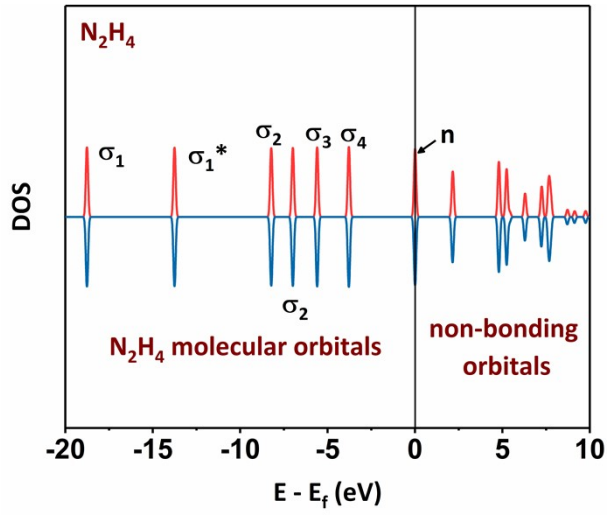

Figure S45. Density of states (DOS) diagram of the N_2H_4 molecule.

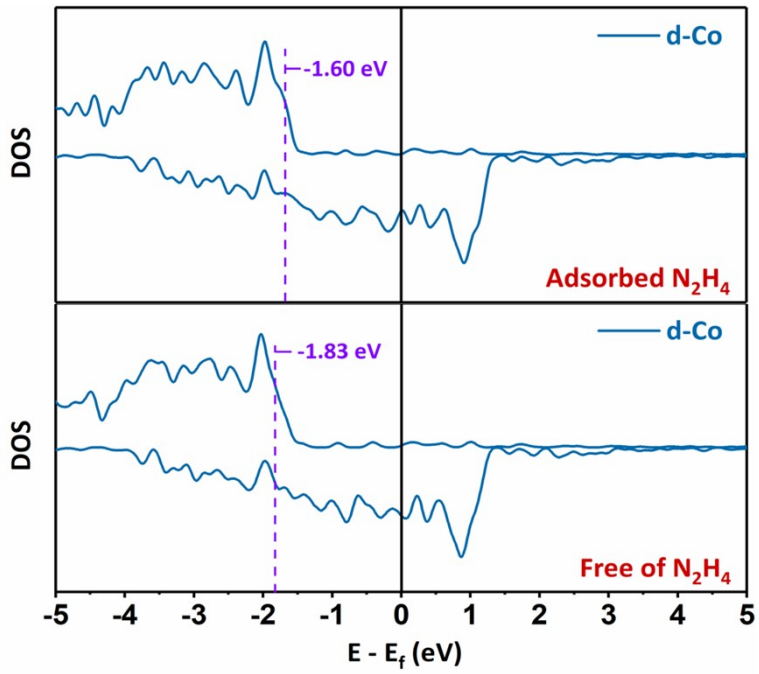

Figure S46. The d-band of DOS for Co (101) and N_2H_4 adsorbed Co (101). The dotted line marks the position of d-band center.

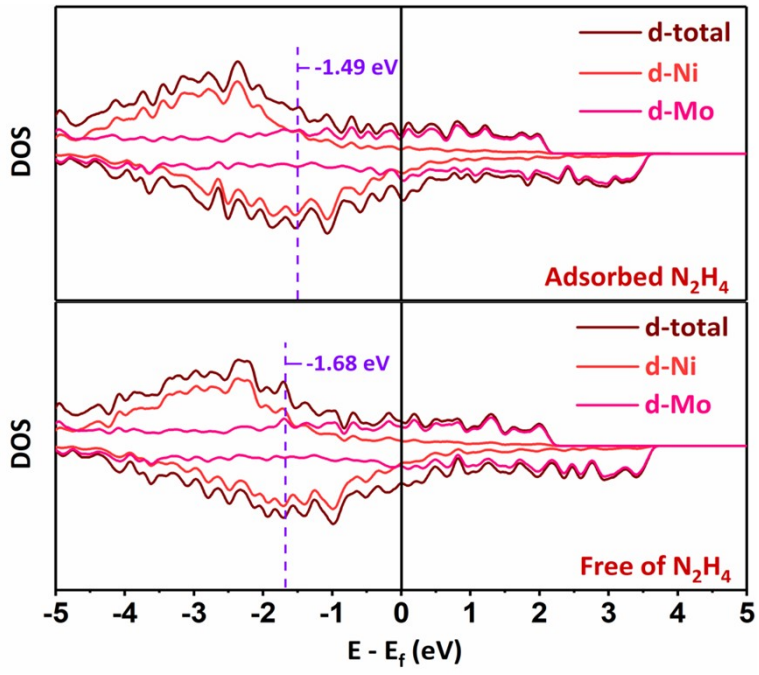

Figure S47. The d-band of DOS for MoNi (133) and N_2H_4 adsorbed MoNi (133). The dotted line marks the position of d-band center.

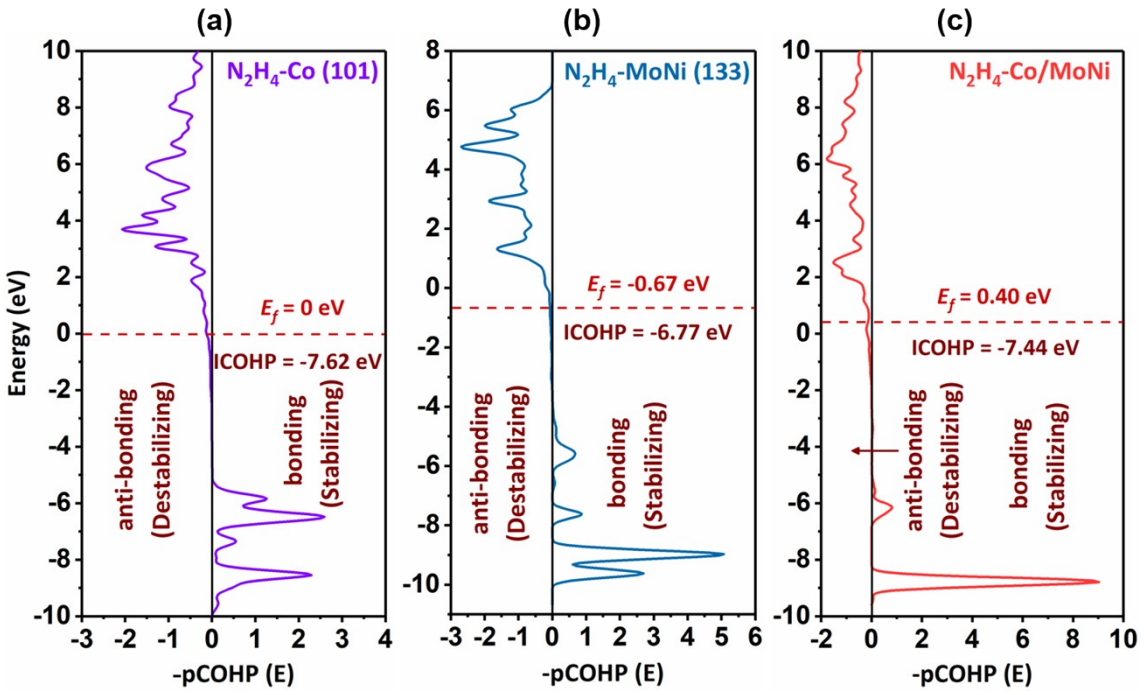

Figure S48. Calculated crystal orbital Hamilton population (COHP) for N_2H_4 adsorbed Co (101), N_2H_4 adsorbed MoNi (133) and N_2H_4 adsorbed Co/MoNi. Positive and negative denote bonding (stabilizing) and antibonding (destabilizing) orbital interactions, respectively. The dotted line marks the position of Fermi energy level.

Table S1. Comparison of the CoNiMo/CoNiMoO_x catalyst with previously reported catalysts in HzOR performance.

Catalyst	Current density (mA·cm^{-2}) at 0 V (vs. RHE)	Potential (V) at 100 mA·cm^{-2}	Reference
CoNiMo/CoNiMoO_x	**164.9**	**-0.023**	**This work**
Co/LaCoO_x@N-C	20	0.58	6
V-Ni_3N NS	8	0.04	7
CoP/Co	30	0.177	8
Ni(Cu)/NF	10	0.06	9
NiCo-$MoNi_4$ HMNAs	40	0.055	10
Ni_2P-HNTs	0.15	0	11
Ni(Cu) CNPs	5	0.339	12

Table S2. Comparison of the CoNiMo/CoNiMoO_x catalyst with previously reported catalysts in HER performance.

Catalyst	Overpotential (mV) at 100 mA·cm^{-2}	Tafel slope (mV·dec^{-1})	Reference
CoNiMo/CoNiMoO_x	**79**	**12.6**	**This work**
NiCo-MoNi_4 HMNAs	205	67.5	10
FeNiP/MoO_x/NiMoO_4	97	27.2	13
NF-CMP-350	197	93	14
NiMoO_4/Ni$(OH)_2$	290	97	15
N-NiMoO_4/Ni_3N	112	45.57	16
CoMoS/CoMoO_4	275	69	17
NiMoO_{4-x}/MoO_2	106	31	18

Table S3. Comparison of the CoNiMo/CoNiMoO$_x$ catalyst assembled hybrid seawater electrolyzer with previously reported state-of-the-art overall water splitting systems in cell performance.

Cell system	Electrolyte	Current density (mA·cm^{-2})	Cell voltage (V)	Power consumption (kWh·m^{-3}H$_2$)	Reference
CoNiMo/CoNiMoO$_x$	**1.0 M NaOH + 0.5 M N$_2$H$_4$ (+) ‖1.0 M NaOH + 0.5 M NaCl(-)**	**100**	**0.059**	**0.143**	**This work**
NiFe LDH (+) ‖ Ni-P-O (-)	1.0 M KOH + 0.5 M NaCl	60	1.546	3.695	19
NiFe LDH (+) ‖ FeNiP/MoO$_x$ (-)	1.0 M KOH + 0.5 M NaCl	30	1.53	3.657	13
Ni$_2$P-Fe$_2$P	1.0 M KOH + seawater	100	1.811	4.328	20
CoP$_x$@FeOOH (+) ‖ CoP$_x$ (-)	1.0 M KOH + seawater	10	1.549	3.702	21
NiFe LDH/CF (+) ‖ NiFeP/Cu$_{NW}$/CF (-)	1.0 M KOH + 0.5 M NaCl	10	1.4	3.346	22
MoS$_2$/Co$_9$S$_8$/Ni$_3$S$_2$	1.0 M KOH	50	1.82	4.35	23
NiMoN@NiFeN	1.0 M KOH + seawater	100	1.581	3.779	24
Fe-NiMoN	1.0 M KOH + seawater	10	1.449	3.463	25
Ni-MoN	1.0 M KOH + seawater	100	1.635	3.908	26
S-(Ni, Fe)OOH (+) ‖ NiMoN (-)	1.0 M KOH + 0.5 M NaCl	100	1.661	3.97	27
MoO$_3$/Ni-NiO	1.0 M KOH	30	1.62	3.872	28
(Ni, Fe)OOH (+) ‖ MoNi$_4$ (-)	1.0 M KOH	50	1.464	3.5	29
h-NiMoFe	1.0 M KOH	100	1.43	3.418	30

Table S4. Comparisons of the alkaline hydrazine-assisted water splitting performance with recently reported cell systems.

Cell system	Voltage at η_{100} (V)	Reference
CoNiMo/CoNiMoO_x	**0.059**	**This work**
V-Ni_3N NS	0.392	7
Ni(Cu)/NF	0.41	9
NiCo/$MoNi_4$ HMNAs	0.315	10
Ni(Cu) CNPs	0.339	12
NiSe/NF	0.52	31
Co_3O_4/Co	0.19	32
Co_xP@Co_3O_4	0.24	33
MoO_2/Co-NF	0.319	34
Ni/β-$Ni(OH)_2$	0.38	35
Ni_2P/Zn-Ni-P	0.358	36
PW-Co_3N NWA/NF	0.501	37
Ni_3N-Co_3N PNAs	0.668	38
CoP/TiM	0.56	39

Table S5. Detailed lattice information of Co (101), MoNi (133) and Co/MoNi heterostructure.

Structure	Lattice parameters		Misfit rate	Formation energy (eV)
	a	b		
Co (101)	14.0371	10.0031	/	/
MoNi (133)	13.4681	12.3143	/	/
Co/MoNi	13.9581	11.7871	3.638%	-1.659

References

1 G. Kresse, J. Furthmüller, *Comp. Mater. Sci.*, 1996, **6**, 15-50.

2 G. Kresse, J. Furthmüller, *Phys. Rev. B*, 1996, **54**, 11169-11186.

3 J. P. Perdew, K. Burke, M. Ernzerhof, *Phys. Rev. Lett.*, 1996, **77**, 3865-3868.

4 G. Kresse, D. J. P. R. B. C. M. Joubert, *Phys. Rev. B*, 1999, **59**, 1758-1775.

5 P. E. J. P. r. B. Blchl, *Phys. Rev. B*, 1994, **50**, 17953-17979.

6 L. Gao, J. Xie, S. Liu, S. Lou, Z. Wei, X. Zhu, B. Tang, *ACS Appl. Mater. Inter.*, 2020, **12**, 24701-24709.

7 J. Zhang, Y. Liu, J. Li, X. Jin, Y. Li, Q. Qian, Y. Wang, A. El-Harairy, Z. Li, Y. Zhu, H. Zhang, M. Cheng, S. Zeng, G. Zhang, *ACS Appl. Mater. Inter.*, 2021, **13**, 3881-3890.

8 S. Chen, C. Wang, S. Liu, M. Huang, J. Lu, P. Xu, H. Tong, L. Hu, Q. Chen, *J. Phys. Chem. Lett.*, 2021, **12**, 4849-4856.

9 Q. Sun, L. Wang, Y. Shen, M. Zhou, Y. Ma, Z. Wang, C. Zhao, *ACS Sustain. Chem. Eng.*, 2018, **6**, 12746-12754.

10 Q. Qian, Y. Li, Y. Liu, Y. Guo, Z. Li, Y. Zhu, G. Zhang, *Chem. Eng. J.*, 2021, **414**, 128818.

11 T.-J. Wang, G.-R. Xu, H.-Y. Sun, H. Huang, F.-M. Li, P. Chen, Y. Chen, *Nanoscale*, 2020, **12**, 11526-11535.

12 Q. Sun, Y. Li, J. Wang, B. Cao, Y. Yu, C. Zhou, G. Zhang, Z. Wang, C. Zhao, *J. Mater. Chem. A*, 2020, **8**, 21084-21093.

13 Z. Xiao, M. Yang, J. Wang, Z. Xu, S. Zhang, A. Tang, R. Gao, H. Yang, *Appl. Catal. B*, 2022, **303**, 120913.

14 S. Zhao, J. Berry-Gair, W. Li, G. Guan, M. Yang, J. Li, F. Lai, F. Corà, K. Holt, D. J. L. Brett, G. He, I. P. Parkin, *Adv. Sci.*, 2020, **7**, 1903674.

15 S. Hu, H. Wu, C. Feng, Y. Ding, *Int. J. Hydrog. Energy*, 2020, **45**, 21040-21050.

16 X. Liu, Y. Guo, P. Wang, Q. Wu, Q. Zhang, E. A. Rozhkova, Z. Wang, Y. Liu, Z. Zheng, Y. Dai, B. Huang, *ACS Appl. Energy Mater.*, 2020, **3**, 2440-2449.

17 Y.-R. Liu, X. Shang, W.-K. Gao, B. Dong, X. Li, X.-H. Li, J.-C. Zhao, Y.-M. Chai, Y.-Q. Liu, C.-G. Liu, *J. Mater. Chem. A*, 2017, **5**, 2885-2896.

18 Z. Zhang, X. Ma, J. Tang, *J. Mater. Chem. A*, 2018, **6**, 12361-12369.

19 Z. Xiao, M. Yang, C. Liu, B. Wang, S. Zhang, J. Liu, Z. Xu, R. Gao, J.-J. Zou, A. Tang, H. Yang, *Nano Energy*, 2022, **98**, 107233.

20 L. Wu, L. Yu, F. Zhang, B. McElhenny, D. Luo, A. Karim, S. Chen, Z. Ren, *Adv. Funct. Mater.*, 2021, **31**, 2006484.

21 L. Wu, L. Yu, B. McElhenny, X. Xing, D. Luo, F. Zhang, J. Bao, S. Chen, Z. Ren, *Appl. Catal. B*, 2021, **294**, 120256.

22 A. Kumar, V. Q. Bui, J. Lee, A. R. Jadhav, Y. Hwang, M. G. Kim, Y. Kawazoe, H. Lee, *ACS Energy Lett.*, 2021, **6**, 354-363.

23 Y. Yang, H. Yao, Z. Yu, S. M. Islam, H. He, M. Yuan, Y. Yue, K. Xu, W. Hao, G. Sun, H. Li, S. Ma, P. Zapol, M. G. Kanatzidis, *J. Am. Chem. Soc.*, 2019, **141**, 10417-10430.

24 L. Yu, Q. Zhu, S. Song, B. McElhenny, D. Wang, C. Wu, Z. Qin, J. Bao, Y. Yu, S. Chen, Z. Ren, *Nat. Commun.*, 2019, **10**, 5106.

25 M. Ning, F. Zhang, L. Wu, X. Xing, D. Wang, S. Song, Q. Zhou, L. Yu, J. Bao, S. Chen, Z. Ren, *Energy Environ. Sci.*, 2022, **15**, 3945-3957.

26 L. Wu, F. Zhang, S. Song, M. Ning, Q. Zhu, J. Zhou, G. Gao, Z. Chen, Q. Zhou, X. Xing, T. Tong, Y. Yao, J. Bao, L. Yu, S. Chen, Z. Ren, *Adv. Mater.*, 2022, **34**, 2201774.

27 L. Yu, L. Wu, B. McElhenny, S. Song, D. Luo, F. Zhang, Y. Yu, S. Chen, Z. Ren, E*nergy Environ. Sci.*, 2020, **13**, 3439-3446.

28 X. Li, Y. Wang, J. Wang, Y. Da, J. Zhang, L. Li, C. Zhong, Y. Deng, X. Han, W. Hu, *Adv. Mater.*, 2020, **32**, 2003414.

29 H. Zhou, F. Yu, Q. Zhu, J. Sun, F. Qin, L. Yu, J. Bao, Y. Yu, S. Chen, Z. Ren, *Energy Environ. Sci.*, 2018, **11**, 2858-2864.

30 Y. Luo, Z. Zhang, F. Yang, J. Li, Z. Liu, W. Ren, S. Zhang, B. Liu, *Energy Environ. Sci.*, 2021, **14**, 4610-4619.

31 Y. Li, Y. Zhao, F.-M. Li, Z. Dang, P. Gao, *ACS Appl. Mater. Inter.*, 2021, **13**, 34457-34467.

32 X. Xu, T. Wang, L. Dong, W. Lu, X. Miao, *ACS Sustain. Chem. Eng.*, 2020, **8**, 7973-7980.

33 X. Xu, T. Wang, W. Lu, L. Dong, H. Zhang, X. Miao, *ACS Sustain. Chem. Eng.*, 2021, **9**, 4688-4701.

34 Y. Guo, X. Liu, Y. Zang, Y. Wu, Q. Zhang, Z. Wang, Y. Liu, Z. Zheng, H. Cheng, B. Huang, Y. Dai, P. Wang, *J. Mater. Chem. A*, 2022, **10**, 17297-17306.

35 D. Shao, Q. Wang, X. Yao, Y. Zhou, X.-Y. Yu, *J. Mater. Chem. A*, 2022, **10**, 21848-21855.

36 Y. Li, X. Yu, J. Gao, Y. Ma, *J. Mater. Chem. A*, 2023, **11**, 2191-2202.

37 Y. Liu, J. Zhang, Y. Li, Q. Qian, Z. Li, Y. Zhu, G. Zhang, *Nat. Commun.*, 2020, **11**, 1853.

38 Q. Qian, J. Zhang, J. Li, Y. Li, X. Jin, Y. Zhu, Y. Liu, Z. Li, A. El-Harairy, C. Xiao, G. Zhang, Y.

Xie, *Angew. Chem. Int. Ed.*, 2021, **60**, 5984-5993.

39 J. Wang, R. Kong, A. M. Asiri, X. Sun, *ChemElectroChem*, 2017, **4**, 481-484.